# Real-Space Imaging of the Tailored Plasmons in Twisted Bilayer Graphene

F. Hu,[1,2] Suprem R. Das,[2,3,4,5] Y. Luan,[1,2] T.-F. Chung,[6,7] Y. P. Chen,[6,7,8,9] and Z. Fei[1,2,*]

[1]*Department of Physics and Astronomy, Iowa State University, Ames, Iowa 50011, USA*
[2]*Ames Laboratory, U.S. Department of Energy, Iowa State University, Ames, Iowa 50011, USA*
[3]*Department of Mechanical Engineering, Iowa State University, Ames, Iowa 50011, USA*
[4]*Department of Industrial and Manufacturing Systems Engineering, Kansas State University, Manhattan, Kansas 66506, USA*
[5]*Department of Electrical and Computer Engineering, Kansas State University, Manhattan, Kansas 66506, USA*
[6]*Birck Nanotechnology Center, Purdue University, West Lafayette, Indiana 47907, USA*
[7]*Department of Physics and Astronomy, Purdue University, West Lafayette, Indiana 47907, USA*
[8]*School of Electrical and Computer Engineering, Purdue University, West Lafayette, Indiana 47907, USA*
[9]*Purdue Quantum Center, Purdue University, West Lafayette, Indiana 47907, USA*

We report a systematic plasmonic study of twisted bilayer graphene (TBLG)—two graphene layers stacked with a twist angle. Through real-space nanoimaging of TBLG single crystals with a wide distribution of twist angles, we find that TBLG supports confined infrared plasmons that are sensitively dependent on the twist angle. At small twist angles, TBLG has a plasmon wavelength comparable to that of single-layer graphene. At larger twist angles, the plasmon wavelength of TBLG increases significantly with apparently lower damping. Further analysis and modeling indicate that the observed twist-angle dependence of TBLG plasmons in the Dirac linear regime is mainly due to the Fermi-velocity renormalization, a direct consequence of interlayer electronic coupling. Our work unveils the tailored plasmonic characteristics of TBLG and deepens our understanding of the intriguing nano-optical physics in novel van der Waals coupled two-dimensional materials.

Graphene Dirac plasmons [1–6], which are collective oscillations of Dirac fermions in graphene, have been widely investigated in recent years by using both the electron energy loss spectroscopy [7–9] and optical imaging or spectroscopy [10–21] techniques. These quasiparticles demonstrate many superior characteristics including high confinement, long lifetime, strong field enhancement, electrical tunability, and a broad spectral range from terahertz to infrared [1–21]. So far, plasmons in single-layer graphene (SLG) have been extensively studied and are generally well understood. One convenient way to create new plasmonic materials with novel physics and properties is by stacking graphene with graphene or other 2D materials into van der Waals (vdW) materials or heterostructures. Indeed, the 2D nature of graphene makes it extremely sensitive to interlayer coupling that could dramatically modify the properties of Dirac fermions and their plasmonic excitations. For example, earlier studies about Bernal-stacked bilayer graphene (BLG) [20,22] and graphene/hBN heterostructures [23,24] have demonstrated many unique plasmonic characteristics compared to those of SLG.

In this Letter, we report a systematic nanoinfrared imaging study of plasmons in twisted bilayer graphene (TBLG) [Fig. 1(a)], which is formed when two misoriented graphene layers are stacked together by vdW forces. Depending on the twist angle ($\theta$) between the two graphene layers, moiré patterns with different periodicities could form [Fig. 1(b)]. Because of the interlayer coupling and modulation of Dirac

fermions by the moiré superlattice potential, the electronic structure of TBLG shows distinct features compared to SLG and Bernal-stacked BLG, and it varies systematically with $\theta$. For example, TBLG with a sizable $\theta$ features two separated Dirac cones [Fig. 1(c)] in the momentum space [25–34]. Moreover, the Fermi velocity ($v_F^{\mathrm{TBLG}}$) close to the charge neutrality point is renormalized compared to that of SLG ($v_F^{\mathrm{SLG}}$); namely, $v_F^{\mathrm{TBLG}}$ drops systematically below $v_F^{\mathrm{SLG}}$ as $\theta$ decreases [25–30]. Therefore, TBLG is a unique system where the Fermi velocity of Dirac fermions could become an adjustable variable in experimental studies. The unique electronic properties of TBLG have led to observations of many interesting optical phenomena through far-field spectroscopic experiments [35–38]. So far, plasmonic responses of TBLG have not been explored experimentally despite the potential rich physics according to theoretical predictions [39,40].

Here we utilize a scattering-type scanning near-field optical microscope (s-SNOM) to perform nanoinfrared imaging studies of TBLG plasmons. The s-SNOM apparatus is built based on an atomic force microscope (AFM). As illustrated in Fig. 1(a), the infrared light (solid arrow) from a continuous-wave infrared laser is focused at the apex of a metalized AFM tip. The laser-illuminated tip acts as both a launcher and a detector of surface plasmons [13–23]. The backscattered light (dashed arrow) off the tip-sample system contains essential information about plasmons underneath the tip. The s-SNOM collects
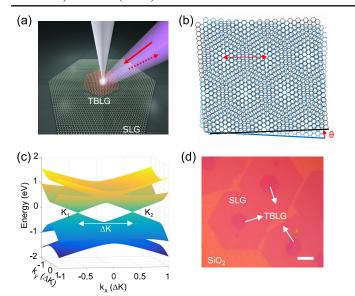
FIG. 1. (a) Illustration of the nanoinfrared imaging experiment of a TBLG single crystal. The solid and dashed arrows mark the directions of the incident laser beam and backscattered photons, respectively. (b) Sketch of the crystal structure of TBLG revealing the moiré periodic pattern. The double-sided arrow marks the moiré period. (c) Calculated band structure of TBLG with a twist angle of 5° with the continuum model [25]. Here the momentum unit $\Delta K$ equals the separation between the two Dirac points ($K_1$ and $K_2$) in the momentum space. (d) Optical image of representative TBLG and SLG single-crystal samples. The scale bar represents 5 $\mu$m.

simultaneously the topography, near-field scattering amplitude ($s$), and phase ($\psi$). By analyzing both the $s$ and $\psi$ data images, we can determine the key plasmonic parameters of TBLG. Our samples were grown by the chemical

vapor deposition (CVD) method on copper foils [41–43] and then transferred to the standard $SiO_2$/Si substrates (Supplemental Material [44]). As shown in Fig. 1(d), both SLG and TBLG are single-crystal grains with a hexagonal shape, and the TBLG grains are typically located at the center of relatively larger SLG grains. Occasionally, we also see hexagonlike shapes with slightly curved edges (Fig. S5) [45,46], but in all cases, these SLG or TBLG single crystals demonstrate a sixfold rotational symmetry (Supplemental Material [44]). According to the previous studies [45,47], the sixfold flake symmetry correlates strictly and accurately with the lattice orientation, so it is convenient to determine the twist angle with a relatively good accuracy ($\pm1°$) by comparing the orientations of the TBLG and SLG grains.

Representative s-SNOM imaging data are shown in Fig. 2, where we plot both the normalized amplitude [Fig. 2(b)] and phase [Fig. 2(c)] signals of a typical sample region containing two TBLG grains. The data images were taken at an excitation laser energy of $E = 0.11$ eV that is away from the strong optical phonon resonance of $SiO_2$ centered at about 0.14 eV [13]. Therefore, the near-field responses of graphene at our excitation energy are mainly due to plasmons [14]. Figure 2(a) sketches the sample configuration, where we can conveniently determine the twist angles of TBLG from the orientations of the hexagonal grains. For example, the TBLG sample labeled as "TBLG1" has a twist angle of about 26° relative to SLG, and the one labeled as "TBLG2" has a twist angle close to 1°. Their different twist angles result in distinct near-field responses. As shown in Figs. 2(b) and 2(c), TBLG1 has a significantly higher near-field amplitude compared to SLG but shows no clear phase contrast with respect to the latter.
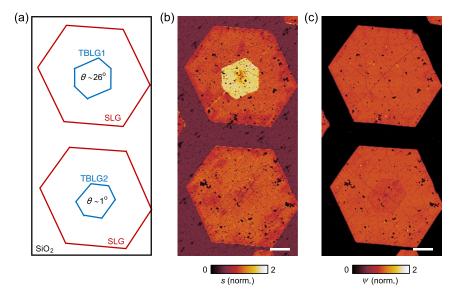


FIG. 2. (a) Sketch of the sample geometry indicating two adjacent TBLG grains with different twist angles with respect to SLG. (b),(c) The near-field images plotting the scattering amplitude ($s$) and phase ($\psi$), respectively. In both images, the amplitude or phase signal is normalized to that of SLG. The laser energy is set to be at $E = 0.11$ eV. The scale bars represent 3 $\mu$m.
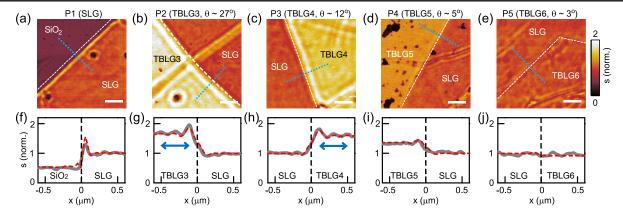
FIG. 3. (a)–(e) High-resolution near-field amplitude images of the five small regions ($P1$–$P5$) marked in Fig. S1 (squares), respectively. The white dashed lines in the images mark the SLG edge and the TBLG-SLG boundaries. The scale bars represent 400 nm. (f)–(j) Experimental (gray solid line) and modeled (red dashed line) amplitude profiles taken along the blue dashed lines in the corresponding near-field images above. The blue arrows in (g) and (h) mark the size of $\lambda_p^{\mathrm{TBLG}}$ that is twice the fringe period. The vertical dashed lines mark the boundaries between SLG and TBLG.

On the contrary, the amplitude of TBLG2 is almost the same as that of SLG, and its phase is slightly weaker. Such dramatic differences in the near-field responses are clear indications of the strong $\theta$ dependence of TBLG. More near-field data images are given in Figs. S1 and S2, where additional TBLG samples with various twist angles are shown. In all the samples we measured (partly shown in Figs. 2, S1, and S2), the near-field amplitude of TBLG is comparable to SLG for $\theta \leq 3°$ and gradually increases from an intermediate signal ($\theta \approx 5°$) to a maximum value ($\theta > 7°$). The phase signal of TBLG, on the other hand, is roughly the same as SLG for $\theta > 7°$ but slightly declines as $\theta$ approaches 0°. The above $\theta$ dependence is more clearly seen in Figs. 4(c) and 4(d), where we summarized the extracted amplitude and phase signal data points (squares) from tens of TBLG samples that we measured.

The unique near-field responses discussed above are directly linked to the plasmons in TBLG. Indeed, we found direct evidence of plasmons in the high-resolution imaging data (Figs. 3 and S3) taken over five small sample regions (marked with dashed squares) in Fig. S1. These regions (labeled with "$P1$"–"$P5$") are chosen to be at the edge of SLG or the boundaries between SLG and TBLG. The amplitude images are shown in Figs. 3(a)–3(e), where we observe bright fringe(s) close to the SLG edge and the SLG-TBLG boundaries. This can be seen more clearly in the line profiles [gray solid curves in Figs. 3(f)–3(j)] taken perpendicular to the edges or boundaries in the amplitude images (along blue dashed lines). Here in these line profiles, the peak features correspond to the bright fringes in the images.

According to previous studies [14–24], the bright fringes registered by the s-SNOM are generated due to the constructive interference between tip-launched and edge- or boundary-reflected plasmons. The plasmonic origin of the observed fringes is further confirmed by the spectroscopic imaging data (Fig. S4), where we observed a systematic

evolution of the bright fringes with laser energy, consistent with the dispersion nature of plasmons. There are two main observations from these plasmonic fringes data (Fig. 3). First, fringes are clear and strong close to the SLG-TBLG3 ($\theta \approx 27°$) and SLG-TBLG4 ($\theta \approx 12°$) boundaries. As $\theta$ decreases, the fringes become weaker and fewer at the SLG-TBLG5 ($\theta \approx 5°$) boundary and then barely seen at the SLG-TBLG6 boundary ($\theta \approx 3°$). Second, in the case of SLG-TBLG3 [Fig. 3(b)] and SLG-TBLG4 [Fig. 3(c)] boundaries, we can easily identify two to three fringes. Nevertheless, at the edge of SLG [Fig. 3(a)], we can see only one bright fringe. Note that the edge of SLG is a nearly perfect plasmon reflector. The plasmon reflection at the SLG-TBLG boundaries, on the other hand, is in principle weaker. Therefore, we can tell directly from the fringe data that our SLG sample has a relatively higher plasmon damping compared to TBLG with relatively large $\theta$. Figure S3 plots the near-field phase images and the corresponding line profiles, where plasmonic interference fringes are also seen. The amplitude and phase imaging data are consistent and complementary to each other. They are all considered in our modeling as discussed in detail below.

To extract quantitative information about plasmons in SLG and TBLG, we performed numerical modeling of both the plasmonic fringes profiles (Figs. 3 and S3) and the $\theta$-dependent near-field amplitude and phase signals [Figs. 4(c) and 4(d)] by using the so-called spheroid model. In this model, the s-SNOM tip is approximated as a highly elongated conducting spheroid (Fig. S7), and we evaluate the complex scattering signal by computing the total radiating dipole of the coupled tip-sample system (Supplemental Material [44]). We emphasize that our model has been proven to be effective in describing s-SNOM responses of graphene with quantitative accuracy [14,16,23]. The main modeling parameter of the sample is the optical conductivity ($\sigma = \sigma_1 + i\sigma_2$) that is directly

linked to the complex plasmon wave vector ($q_p = q_1 + iq_2$) under the long-wavelength approximation:

$$q_p \approx i\varepsilon_0(1 + \varepsilon_s)E/\hbar\sigma. \quad (1)$$

Here $\hbar$ is the reduced Planck constant, $\varepsilon_0$ is the vacuum permittivity, and $\varepsilon_s$ is the relative permittivity of SiO$_2$. For convenience, our analysis and discussions are based on the following two parameters: the plasmon wavelength ($\lambda_p = 2\pi/q_1$) and damping rate ($\gamma_p = q_2/q_1$). Based on Eq. (1), we know that the plasmon wavelength ($\lambda_p$) is roughly proportional to $\sigma_2$, and the damping rate ($\gamma_p$) scales linearly with $\sigma_1/\sigma_2$.

We first fit the plasmonic fringe profiles of SLG [Figs. 3(f) and S3(f)]. Through the fitting, we extract the plasmon wavelength ($\lambda_p^{\mathrm{SLG}}$) and damping rate ($\gamma_p^{\mathrm{SLG}}$) of SLG at $E = 0.11$ eV to be about 279 nm and 0.2, respectively. Based on Eq. (1), we can establish a simple relation between $\lambda_p^{\mathrm{SLG}}$ and the carrier density ($n$) under the Drude approximation:

$$\lambda_p^{\mathrm{SLG}} \approx \frac{2e^2\hbar v_F^{\mathrm{SLG}}\sqrt{\pi|n|}}{(1 + \varepsilon_s)\varepsilon_0 E^2}. \quad (2)$$

Here $v_F^{\mathrm{SLG}} \approx 10^6$ m/s is the Fermi velocity of SLG. Equation (2) allows us to estimate the carrier density of SLG to be $n \approx 1.2 \times 10^{13}$ cm$^{-2}$, which is a typical value for highly hole-doped CVD samples on SiO$_2$/Si substrates at ambient conditions [16]. The relatively high doping is mainly due to the impurities on the surface of SiO$_2$ as well as the water and oxygen molecules in the air [48]. Considering that all the samples studied here share the same substrate and atmospheric conditions, they are expected to share roughly an equal density of external dopants and therefore a similar carrier density [21,22].

Based on the extracted parameters of SLG, we then determine both the plasmon wavelength ($\lambda_p^{\mathrm{TBLG}}$) and damping rate ($\gamma_p^{\mathrm{TBLG}}$) of TBLG by fitting the fringe profiles at the SLG-TBLG boundaries (Figs. 3 and S3). Through fitting, we estimate that ($\lambda_p^{\mathrm{TBLG}}$, $\gamma_p^{\mathrm{TBLG}}$) of TBLG3 ($\theta \approx 27°$), TBLG4 ($\theta \approx 12°$), TBLG5 ($\theta \approx 5°$), and TBLG6 ($\theta \approx 3°$) to be (393 nm, 0.10), (387 nm, 0.11), (340 nm, 0.16), and (278 nm, 0.28), respectively. These numbers are plotted in Figs. 4(a) and 4(b) as data points. Note that the first two numbers of $\lambda_p^{\mathrm{TBLG}}$ can be read out directly from the fringe profiles of TBLG3 and TBLG4 by doubling the fringe period [arrows in Figs. 3(g) and 3(h)]. Nevertheless, precise modeling of the complex fringe profiles is required to extract both $\lambda_p^{\mathrm{TBLG}}$ and $\gamma_p^{\mathrm{TBLG}}$ and to analyze data from TBLG samples without strong fringes [Figs. 3(d) and 3(e)]. In the latter case, the modeling fits mainly the $s$ and $\psi$ signals of TBLG in contrast to SLG. In Figs. 4(c) and 4(d), we show the modeling curves of $s$ and $\psi$ contrast signals of TBLG versus SLG at a wide distribution of twist angles (red curves), which match well the trend of the

experimental data points with twist angles above 3° (marked with dashed lines). At twist angles below 3°, the experimental data points clearly deviate from the modeling curve, which will be discussed in the following paragraphs. The smooth $\lambda_p^{\mathrm{TBLG}}(\theta)$ and $\gamma_p^{\mathrm{TBLG}}(\theta)$ parameters [red curves in Figs. 4(a) and 4(b)] used to model the $s$ and $\psi$ contrast signals are fully consistent with the discrete data points obtained from fringe profile fitting.

Now we discuss the origin of the $\theta$ dependence of $\lambda_p^{\mathrm{TBLG}}$ and $\gamma_p^{\mathrm{TBLG}}$. We first pay attention to twist angles above 3°, where TBLG is in the Dirac regime [Fig. 1(c)] [25–29]. Here we assume that carriers are equally distributed among the two graphene layers, which is reasonable considering no external gating. The general results will not change much even with slightly unequal carrier distribution among the two graphene layers (Fig. S6 and Supplemental Material [44]). Under the equal carrier distribution assumption, $\lambda_p^{\mathrm{TBLG}}$ can be written as

$$\lambda_p^{\mathrm{TBLG}}(\theta) \approx \frac{2e^2\hbar\sqrt{2\pi|n|}}{(1 + \varepsilon_s)\varepsilon_0 E^2}v_F^{\mathrm{TBLG}}(\theta), \quad (3)$$

where the Fermi velocity of TBLG ($v_F^{\mathrm{TBLG}}$) is proven to be sensitively dependent on $\theta$ due to the Fermi velocity renormalization. The amount of Fermi velocity renormalization is determined by the interlayer coupling energy ($t$)
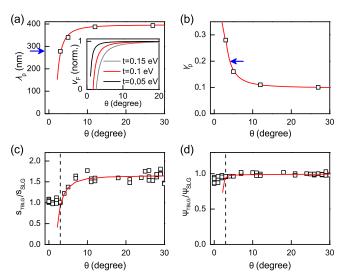


FIG. 4. (a) The $\lambda_p^{\mathrm{TBLG}}$ data points extracted by modeling the fringe profiles in Fig. 3. The inset plots the calculated $v_F^{\mathrm{TBLG}}(\theta)$ normalized to $v_F^{\mathrm{SLG}}(\theta)$ considering different $t$. (b) The $\gamma_p^{\mathrm{TBLG}}$ data points extracted by modeling the fringe profiles in Fig. 3. The red curves in (a) and (b) are used for calculations of the amplitude and phase signals in (c) and (d). The blue arrows in (a) and (b) mark the values of $\lambda_p^{\mathrm{SLG}}$ and $\gamma_p^{\mathrm{SLG}}$, respectively. (c) The $\theta$-dependent near-field amplitude from both experiment (squares) and modeling (red curve). (d) The $\theta$-dependent near-field phase from both experiment (squares) and modeling (red curve). Both the amplitude (c) and phase (d) of TBLG are normalized to those of SLG. The vertical dashed lines in (c) and (d) mark $\theta = 3°$.

of TBLG [inset in Fig. 4(a)] as described by the following equation [25]:

$$v_F^{\text{TBLG}}(\theta) = v_F^{\text{SLG}}\left[1 - 9\left(\frac{t}{\hbar v_F^{\text{SLG}}\Delta K}\right)^2\right]. \quad (4)$$

Here, $\Delta K = (8\pi/3a)\sin(\theta/2)$ is the momentum separation of the two Dirac cones [Fig. 1(c)], and $a = 0.346$ nm is the lattice constant. Equation (4) indicates that $t$ is the one single parameter that controls $v_F^{\text{TBLG}}(\theta)$ and hence $\lambda_p^{\text{TBLG}}(\theta)$. Here we set $t$ to be 0.1 eV, which is roughly consistent with previous studies [29,34]. With such a $t$ setting, we calculated $\lambda_p^{\text{TBLG}}(\theta)$ based on Eqs. (3) and (4), which is shown as the red curve in Fig. 4(a). Other choices of $t$ will lead to either a faster or slower decreasing of $v_F^{\text{TBLG}}$ and hence $\lambda_p^{\text{TBLG}}$ as $\theta$ drops [inset in Fig. 4(a)].

The origin for the higher $\gamma_p^{\text{TBLG}}$ at smaller $\theta$ in the Dirac regime $(\theta \geq 3°)$ is likely due to the stronger charge scattering rates [49,50]. According to previous literature [51], the charge scattering rates ($\Gamma$) due to either long-range Coulomb scattering or short-range defect scattering are inverse proportional to the Fermi velocity. Therefore, as $\theta$ decreases, $\Gamma$ rises and thus $\gamma_p^{\text{TBLG}}$ increases. Note that interband transitions are forbidden due to the Pauli blocking for $\theta \geq 3°$, where the threshold energy for interband transitions $(2E_F^{\text{TBLG}})$ is estimated to be over 0.2 eV, far above our laser energy (0.11 eV).

Finally, we discuss briefly TBLG samples with twist angles below 3°, where the Dirac approximation begins to fail [26–29]. In this regime, we find that the amplitude signal of the TBLG samples deviates from the projected trend of the modeling curves and stays close to that of SLG [Fig. 4(c)]. With quantitative modeling (Fig. S8), we estimate that the $\lambda_p^{\text{TBLG}}$ at small twist angles $(\theta \leq 2°)$ is in the range from 278 to 314 nm. According to previous theoretical studies [26–28], the lowest-energy bands of TBLG with small twist angles become flat or nearly flat close to the charge neutrality point, which could lead to an extremely small $\lambda_p^{\text{TBLG}}$ [Eq. (3)]. The finite $\lambda_p^{\text{TBLG}}$ of TBLG $(\theta \leq 2°)$ observed here suggests that the Fermi surface of our highly doped samples is away from these relatively flat bands. The phase signals [Fig. 4(d)] of TBLG $(\theta \leq 2°)$ appear to be slightly smaller than that of SLG and large-twist-angle TBLG, indicating even higher plasmon damping rates: $\gamma_p^{\text{TBLG}}(\theta \leq 2°) = 0.2$–$0.4$ (Fig. S8). The higher damping is most likely due to interband transitions, which are enabled in TBLG $(\theta \leq 2°)$ at our excitation energy (0.11 eV) due to the small energy separations between the lowest-energy bands. More detailed discussions about TBLG with $\theta \leq 2°$ are given in Supplemental Material [44]. Future studies with more comprehensive experiments of small-twist-angle TBLG and more precise determinations of twist angles are needed to explore further TBLG plasmons in the non-Dirac regime.

By combining the state-of-the-art s-SNOM technique with rigorous numerical modeling, we performed a systematic nanoinfrared imaging study of TBLG single crystals with various twist angles. In the Dirac linear regime, we found that TBLG supports infrared plasmons with parameters that vary systematically with the twist angle between the two graphene planes. The underlining physics behind the observed twist angle dependence is the Fermi velocity renormalization, which is originated from the interlayer electronic coupling. Our study establishes TBLG as a unique platform where the Fermi velocity, the fundamentally important parameter of Dirac fermions, has become an adjustable variable in nano-optical and plasmonic studies of Dirac materials.

F. H., S. R. D., and Y. L. contributed equally to this work.

*Corresponding author.
zfei@iastate.edu

[1] S. Das Sarma and E. H. Hwang, Phys. Rev. Lett. **102**, 206412 (2009).

[2] M. Jablan, H. Buljan, and M. Soljačić, Phys. Rev. B **80**, 245435 (2009).

[3] A. Vakil and N. Engheta, Science **332**, 1291 (2011).

[4] A. N. Grigorenko, M. Polini, and K. S. Novoselov, Nat. Photonics **6**, 749 (2012).

[5] D. N. Basov, M. M. Fogler, and F. J. Garcia de Abajo, Science **354**, aag1992 (2016).

[6] T. Low, A. Chaves, J. D. Caldwell, A. Kumar, N. X. Fang, P. Avouris, T. F. Heinz, F. Guinea, L. Martin-Moreno, and F. Koppens, Nat. Mater. **16**, 182 (2017).

[7] Y. Liu, R. F. Willis, K. V. Emtsev, and Th. Seyller, Phys. Rev. B **78**, 201403(R) (2008).

[8] S. Y. Shin, C. G. Hwang, S. J. Sung, N. D. Kim, H. S. Kim, and J. W. Chung, Phys. Rev. B **83**, 161403(R) (2011).

[9] R. J. Koch, S. Fryska, M. Ostler, M. Endlich, F. Speck, T. Hänsel, J. A. Schaefer, and T. Seyller, Phys. Rev. Lett. **116**, 106802 (2016).

[10] L. Ju et al., Nat. Nanotechnol. **6**, 630 (2011).

[11] H. Yan, X. Li, B. Chandra, G. Tulevski, Y. Wu, M. Freitag, W. Zhu, P. Avouris, and F. Xia, Nat. Nanotechnol. **7**, 330 (2012).

[12] V. W. Brar, M. S. Jang, M. Sherrott, J. J. Lopez, and H. Atwater, Nano Lett. **13**, 2541 (2013).

[13] Z. Fei et al., Nano Lett. **11**, 4701 (2011).

[14] Z. Fei et al., Nature (London) **487**, 82 (2012).

[15] J. Chen et al., Nature (London) **487**, 77 (2012).

[16] Z. Fei *et al.*, Nat. Nanotechnol. **8**, 821 (2013).
[17] G. Woessner *et al.*, Nat. Mater. **14**, 421 (2015).
[18] Z. Fei *et al.* Nano Lett. **16**, 7842 (2016).
[19] F. Hu *et al.* Nano Lett. **17**, 5423 (2017).
[20] J. A. Gerber, S. Berweger, B. T. O'Callahan, and M. B. Raschke, Phys. Rev. Lett. **113**, 055502 (2014).
[21] P. Alonso-González *et al.*, Science **344**, 1369 (2014).
[22] Z. Fei *et al.*, Nano Lett. **15**, 4973 (2015).
[23] G. X. Ni *et al.*, Nat. Mater. **14**, 1217 (2015).
[24] S. Dai *et al.* Nat. Nanotechnol. **10**, 682 (2015).
[25] J. M. B. Lopes dos Santos, N. M. R. Peres, and A. H. Castro Neto, Phys. Rev. Lett. **99**, 256802 (2007).
[26] E. Suárez Morell, J. D. Correa, P. Vargas, M. Pacheco, and Z. Barticevic, Phys. Rev. B **82**, 121407(R) (2010).
[27] G. Trambly de Laissardière, D. Mayou, and L. Magaud, Nano Lett. **10**, 804 (2010).
[28] R. Bistritzer and A. H. MacDonald, Proc. Natl. Acad. Sci. U.S.A. **108**, 12233 (2011).
[29] A. Luican, G. Li, A. Reina, J. Kong, R. R. Nair, K. S. Novoselov, A. K. Geim, and E. Y. Andrei, Phys. Rev. Lett. **106**, 126802 (2011).
[30] L.-J. Yin, J.-B. Qiao, W.-X. Wang, W.-J. Zuo, W. Yan, R. Xu, R.-F. Dou, J.-C. Nie, and L. He, Phys. Rev. B **92**, 201408(R) (2015).
[31] S. Shallcross, S. Sharma, and O. Pankratov, Phys. Rev. B **87**, 245403 (2013).
[32] S. Carr, D. Massatt, S. Fang, P. Cazeaux, M. Luskin, and E. Kaxiras, Phys. Rev. B **95**, 075420 (2017).
[33] G. Li, A. Luican, J. M. B. Lopes dos Santos, A. H. Castro Neto, A. Reina, J. Kong, and E. Y. Andrei, Nat. Phys. **6**, 109 (2010).
[34] W. Yan, M. Liu, R.-F. Dou, L. Meng, L. Feng, Z.-D. Chu, Y. Zhang, Z. Liu, J.-C. Nie, and L. He, Phys. Rev. Lett. **109**, 126801 (2012).

[35] Y. Wang, Z. Ni, L. Liu, Y. Liu, C. Cong, T. Yu, X. Wang, D. Shen, and Z. Shen ACS Nano **4**, 4074 (2010).
[36] X. Zou *et al.*, Phys. Rev. Lett. **110**, 067401 (2013).
[37] R. W. Havener, Y. Liang, L. Brown, L. Yang, and J. Park, Nano Lett. **14**, 3353 (2014).
[38] H. Patel, R. W. Havener, L. Brown, Y. Liang, L. Yang, J. Park, and M. W. Graham, Nano Lett. **15**, 5932 (2015).
[39] T. Stauber, P. San-Jose, and L. Brey, New J. Phys. **15**, 113050 (2013).
[40] T. Stauber and H. Kohler, Nano Lett. **16**, 6844 (2016).
[41] R. He, T.-F. Chung, C. Delaney, C. Keiser, L. A. Jauregui, P. M. Shand, C. C. Chancey, Y. Wang, J. Bao, and Y. P. Chen, Nano Lett. **13**, 3594 (2013).
[42] C.-C. Lu, Y.-C. Lin, Z. Liu, C.-H. Yeh, K. Suenaga, and P.-W. Chiu, ACS Nano **7**, 2587 (2013).
[43] Q. Yu *et al.*, Nat. Mater. **10**, 443 (2011).
[44] See Supplemental Material at http://link.aps.org/supplemental/10.1103/PhysRevLett.119.247402 for additional data and details of experiments and modeling.
[45] B. Wu, D. Geng, Z. Xu, Y. Guo, L. Huang, Y. Xue, J. Chen, G. Yu, and Y. Liu, NPG Asia Mater. **5**, e36 (2013).
[46] Z. Yan *et al.*, Angew. Chem., Int. Ed. **53**, 1565 (2014).
[47] V. Miseikis *et al.*, 2D Mater. **2**, 014006 (2015).
[48] S. Ryu, L. Liu, S. Berciaud, Y.-J. Yu, H. Liu, P. Kim, G. W. Flynn, and L. E. Brus, Nano Lett. **10**, 4944 (2010).
[49] A. Principi, G. Vignale, M. Carrega, and M. Polini, Phys. Rev. B **88**, 121405(R) (2013).
[50] A. Principi, M. Carrega, M. B. Lundeberg, A. Woessner, F. H. L. Koppens, G. Vignale, and M. Polini, Phys. Rev. B **90**, 165408 (2014).
[51] A. H. Castro Neto, F. Guinea, N. M. R. Peres, K. S. Novoselov, and A. K. Geim, Rev. Mod. Phys. **81**, 109 (2009).